Materials Research. 2024; 27:e20240211
DOI: https://doi.org/10.1590/1980-5373-MR-2024-0211

Characterization of Microporous Ceramics Based on Calcium Hexaluminate "In Situ" Produced by Direct Molding

V. M. C. Leite[a], R. Salomão[b], G. L. B. Cardoso[a], F. S. Ortega[a], I. R. Oliveira[a]*

[a]*Universidade do Vale do Paraíba, Instituto de Pesquisa e Desenvolvimento, São José dos Campos, SP, Brasil.*
[b]*Universidade de São Paulo, Escola de Engenharia de São Carlos, São Carlos, SP, Brasil.*

Received: May 05, 2024; Revised: August 20, 2024; Accepted: September 20, 2024

Calcium hexaluminate (CA_6) presents a wide application in high-temperature thermal insulation. Despite the high porosity levels achieved, the use of carbonated precursors in its synthesis inevitably produces CO_2 as a by-product. CA_6 was produced by combining different sources of alumina (α-Al_2O_3 and ρ-Al_2O_3) and lime ($CaCO_3$, $Ca(OH)_2$ and CaO) in aqueous suspensions that were cast and sintered to evaluate these routes on its physical properties. The products attained after sintering at 1550 and 1600 °C were characterized for crystal phases, real density, particle morphology, uniaxial compressive strength, apparent porosity, and pore size distribution. Part of the samples sintered at 1600 °C was subjected to a thermal shock test and was then evaluated for residual strength under diametrical compression, apparent porosity, pore size distribution, and flexural elastic modulus. The CA_6 samples produced from α-Al_2O_3 presented lower pore fraction and higher mechanical strength and modulus of elasticity. The superior properties of the materials produced with α-alumina were maintained after thermal shock. The acicular geometry of the CA_6 particles is related to their excellent thermal shock resistance and mechanical performance. The results indicated a more environmentally friendly system produced from α-Al_2O_3-CaO for industrial applications of high-temperature thermal insulation resistant to thermal shock damage.

Keywords: *Porous ceramics, Calcium hexaluminate, Direct casting, Alumina sources, Calcium oxide sources.*

1. Introduction

Calcium hexaluminate ($CaAl_{12}O_{19}$, $CaO.6Al_2O_3$, or CA_6) is an alumina-rich compound that contains 92 wt% of Al_2O_3 and 7-8 wt% of CaO and presents high thermal stability and refractoriness (melting point higher than 1800°C)[1-6]. Due to this, microporous CA_6-based materials are highly stable in reducing atmospheres and present low solubility in alkaline slag, allowing its contact with molten steel[7-9]. Besides this, its low thermal conductivity (1-4 $W.m^{-1}·K^{-1}$ at 1300 °C)[8-14] and densification[6,15-19] and thermal shock resistance[2,5,8,9,20-22] point out such porous structures as ideal candidates for application as high-temperature thermal insulators[10-19] and hot-air filters[23-25].

Due to their technological importance, during the past 30 years, several works studied the mechanism of porogenesis and solid-state reactions involved in such structure production employing different processing methods. In general terms, CA_6 can be produced from the combination of several sources of Al_2O_3, for instance, calcined alumina (α-Al_2O_3)[2,3,5,6,16,17,19,26-32], hydratable alumina (ρ-Al_2O_3)[33,34], and CaO, such as plain calcium oxide (CaO or lime)[1-4], calcium carbonate (α-$CaCO_3$, or calcite[17,19,21,22,32,34,35], and μ-$CaCO_3$, or vaterite[10]), calcium hydroxide ($Ca(OH)_2$)[34], calcium chlorite ($CaCl_2$)[36,37], and calcium aluminate cement (CAC)[14,18,36-39]. In these studies, frequently the raw materials were dry-mixed and compacted by uniaxial pressing[5,6,16,17,19,26-32], mixed with an organic compound and extruded[35,40,41], or prepared by chemical routes using sol-gel[5,23] or gelcasting techniques[37,40-43] to produce monolith structures[8,9,13,14,33,34], spherical beads[35], or porous aggregates[8,9,11,13,44-46]. After the consolidation of these particles, and during the initial heating up to 900-1000ºC, the decomposition of hydroxylated and carbonated compounds generated empty spaces due to the particles' density mismatch[6,17,19]. Alternatively, foaming agents[47-49] and freeze-casting-based techniques[40] were introduced to increase initial pore content even further. In the 1000-1350ºC temperature range, the solid-state reactions involved in the formation of CA_6 begin at the interface between the Al_2O_3 matrix and CaO domains, where the concentration of Ca^{2+} ions is higher[1,6,10,17,19,50]. Consequently, low-melting point CaO-rich phases ($Ca_3Al_2O_6$ or C_3A, $Ca_{12}Al_{14}O_{33}$ or $C_{12}A_7$, and $CaAl_2O_4$ or CA) form firstly at these contact points[17,19]. As heating continues, these low-melting phases dissolve the neighboring particles, and as the liquid is progressively enriched in alumina, compounds with higher melting points ($CaAl_4O_7$ or CA_2 and CA_6) crystallize. Because typical CA_6 crystals are flat hexagonal plates of high aspect ratio, their formation is expansive and the porosity generated during the decomposition of precursors is partially preserved during sintering[10,16,19].

---

*e-mail: ivonero@univap.br

Once produced and installed in steelmaking equipment, CA_6 structures must withstand thermomechanical stresses resulting from thermal cycling and temperature gradient between the hot and cold faces[8,9,12,13,51]. As the material undergoes successive cycles of thermal shock, its structure accumulates damage, which is a determining factor in its useful life. The increase in size and coalescence of cracks in the material drastically reduces its mechanical strength so failure can occur at stress levels much lower than that supported by the undamaged material[5,9,18,21,22,26,39,52,53]. To minimize thermal shock damage, mineralizer agents, such as SiO_2, MgO, B_2O_3, and SiC were added to the compositions to tune the geometry of CA_6 crystals[54-61]. For instance, whereas SiO_2 additions improved the compacting of the grains and reduced their aspect ratio and inter-particle porosity[54,57,58], the presence of MgO and *in situ* formed magnesium aluminate spinel ($MgAl_2O_4$) generate elongated crystals and compression forces amongst particles that behaved as toughening mechanisms, preventing the formation of long cracks and making this insulating material resistant to thermal shock damage[61,62].

Although the use of calcium carbonate ($CaCO_3$) as a CaO precursor contributes to increasing the porosity, this compound inevitably produces CO_2 as a by-product (between 590 and 753°C)[6,17,19]. Studies show that CaO and $Ca(OH)_2$ are strategic sources of calcium for the production of CA_6, as they release a lower percentage of toxic gases in the final system. In previous works, combinations of α-Al_2O_3 and different calcium oxide sources have been evaluated mainly in processing routes based on uniaxial pressing[10,17,19]. However, they can also be formed by liquid-based routes, such as direct casting. To produce "in situ" CA_6, direct casting requires the production of a stable aqueous co-dispersion of Al_2O_3 and CaO sources' particles after pH adjustment (above 9, to prevent $CaCO_3$ dissolution and avoid aluminas' isoelectric point) and proper dispersion (using poly(sodium-ammonium acrylate)-based dispersants)[6,35]. The high flowability of such suspensions facilitates the casting of parts into complex shapes with large volumes, or even direct application on hot linings[12,13]. Due to this, such a process would present fast application and energy saving[12,13,63]. Because α-Al_2O_3 does not react with water, the addition of a hydraulic binder, such as calcium aluminate cement and hydratable alumina (ρ-Al_2O_3), is necessary to set the suspension before sintering. In both cases, the Al_2O_3-CaO ratio in their particles affects the amount of CA_6 formed[14,33,34].

In comparison, to other processing routes, direct casting was less explored in literature despite its technological importance. In this context, the objective of this work was to produce microporous *in situ* CA_6 by direct casting combinations of alumina (α-Al_2O_3 and ρ-Al_2O_3) and lime sources ($CaCO_3$, $Ca(OH)_2$ and CaO) and to investigate the combined effect of different raw materials and sintering temperature on physical properties (density, crystal phases, microstructure, compressive strength, porosity, pore size distribution, thermal shock resistance).

2. Materials and Methods

2.1. Raw materials and samples preparation

The raw materials used in this work were: calcined alumina (α-Al_2O_3, 3.9 g/cm^3, A1000SG, Almatis, USA), hydraulic alumina (ρ-Al_2O_3, 3.2 g/cm^3, Alphabond 300, Almatis, USA), calcium carbonate ($CaCO_3$, 2.7 g/cm^3, Vetec, Brazil), calcium oxide (CaO, 3.5 g/cm^3, Vetec, Brazil) and calcium hydroxide ($Ca(OH)_2$, 2.2 g/cm^3, Synth, Brazil). The binder used was calcium aluminate cement (CAC, Secar 71, Kerneos). The dispersant additives used were polyglycol) derivative (Castament FS60, Basf) and sodium polymethacrylate (Darvan 7NS, Vanderbilt Minerals). The raw materials were mixed in stoichiometric proportions to produce calcium hexaluminate ($CaAl_{12}O_{19}$, CA_6), represented by Equations 1-3 and defined in Table 1:

$$6Al_2O_3 + CaCO_3 \rightarrow 6Al_2O_3 + CaO + CO_2 \rightarrow CaAl_{12}O_{19} \quad (1)$$

$$6Al_2O_3 + CaO \rightarrow CaAl_{12}O_{19} \quad (2)$$

$$\begin{aligned} &6Al_2O_3 + Ca(OH)_2 \rightarrow 6Al_2O_3 + \\ &CaO + H_2O \rightarrow CaAl_{12}O_{19} \end{aligned} \quad (3)$$

The suspensions were prepared and poured under vibration into cylindrical (16 mm diameter × 18 mm height) and prismatic (75 mm length × 12.5 mm width × 12.5 mm height) molds. After casting, samples were subjected to curing processes (50 °C, 24 h in a saturated environment), drying (110 °C, 24 h), and sintering (1 °C/min up to 1000 °C, 1 h plateau, 5 °C/min. up to 1550 °C or 1600 °C, 2 h plateau, 10 °C/min cooling rate). Such conditions were employed to maximize the binding effect of hydratable alumina and reduce the likelihood of explosive spalling[64].

Samples sintered at 1600 °C also underwent a thermal shock procedure using the thermal fatigue by multiple cycle method, in which the specimens are subjected to several cycles of sudden heating and cooling, keeping the temperature difference fixed at values higher than that necessary to

Table 1. Conditions for preparing aqueous suspensions.

Compositions	Binder (wt%)	Dispersant (wt%)	Solid content (%)
α-Al_2O_3-$CaCO_3$	25	Polyglycol (0.2)	78.0
α-Al_2O_3-CaO	25	Sodium polymethacrylate (2.0)	75.8
α-Al_2O_3-$Ca(OH)_2$	25	Sodium polymethacrylate (1.0)	74.0
ρ-Al_2O_3-$CaCO_3$	-	Polyglycol (1.4)	66.0
ρ-Al_2O_3-CaO	-	Polyglycol (1.6)	57.0
ρ-Al_2O_3-$Ca(OH)_2$	-	Polyglycol (2.8)	54.0

nucleate cracks ($\Delta T_{est} \geq \Delta T_c$). Each sample was inserted for 15 min into an oven at 1025 °C and quickly cooled to room temperature, with a ΔT of approximately 1000 °C. For each sample, 10 cycles were carried out, with a complete cycle being the process of heating and cooling the specimen[65].

2.2. Samples' characterization

The products attained after sintering were characterized for crystal phases, real density, particle morphology, uniaxial compressive strength, apparent porosity, and pore size distribution. Part of the samples sintered at 1600 °C after the thermal shock test were then evaluated for residual strength under diametrical compression, apparent porosity, pore size distribution, and flexural elastic modulus. All tests were carried out on cylindrical samples except for the elastic modulus (in rectangular bars).

X-ray diffraction (XRD-6000, Shimadzu; Cu-Kα radiation = 1.54439 Å) was performed to identify the phases formed and the real density was assessed using an Upyc - 1200, v5.04 (Quantachrome) helium pycnometer. The microstructure at the external surface of the sintered samples was investigated using scanning electron microscopy (SEM, EVO MA10, Zeiss, previously covered by thin gold coating).

The compressive strength (σ_U, MPa) was calculated as the average of 5 specimens of the different CA_6 samples under uniaxial compression, according to ABNT NBR 6224:2001, using a universal testing machine (EMIC DL10.000) with a displacement speed of 0.15 mm/min. The rupture stress of each sample was calculated according to Equation 4:

$$\sigma_U = 4P \;/\; \pi D^2 \tag{4}$$

where P (N) is the load recorded at the fracture of each sample and D is the average diameter of each sample. The diametral compression (σ_D, MPa) test was carried out according to ABNT NBR 7222:2011 using the same equipment and the displacement speed was 0.05 mm/min. The reported value was an average of 5 samples, which residual strength was calculated according to Equation 5:

$$\sigma_D = 2P \;/\; \pi h D \tag{5}$$

where h (mm) is the average height of each sample.

The apparent porosity (AP) and volumetric density (VD) were evaluated following the method based on the Archimedes principle (ASTM C 830). The samples (both green and sintered) in triplicate were initially dry-weighed (M_s). The green and sintered samples were then soaked in kerosene (ρ=0.8 g/cm^3) or water (ρ=1.0 g/cm^3), respectively, under vacuum for 1 h. The immersed (M_i) and wet (M_u) weights were then recorded. The apparent porosity and volumetric density were calculated according to Equations 6 and 7.

$$AP = 100\,\% \times \left[\left(M_U - M_S \right) \;/\; \left(M_U - M_I \right) \right] \tag{6}$$

$$VD = 100\,\% \times \left[M_S \;/\; \left(M_U - M_I \right) \right] \tag{7}$$

The total porosity (TP) was calculated from the ratio between volumetric density (VD) and real density (RD), according to Equation 8, where VD is the ratio between the mass and the external volume and RD was measured by He picnometry, as previously described.

$$TP = 100\,\% \times \left[1 - \left(VD \;/\; RD \right) \right] \tag{8}$$

Pore size distribution was evaluated using the mercury porosimetry technique (Autopore IV 9500, Micromeritics, USA). The diameter of the pore into which mercury penetrates relates to the applied pressure through the Washburn equation (Equation 9), valid for cylindrical pores, where D is the pore diameter, P is the applied pressure, γ is the surface tension of the mercury and ϕ is the contact angle (130°) between the mercury and the sample. The volume of mercury (V) that penetrates the pores is measured directly, as a function of the applied pressure (P). From the curve of the cumulative volume of mercury intruded into the sample after successive pressure increases, the average pore size and pore size distribution can be extracted.

$$D = (-4\gamma cos(\phi)) \;/\; P] \tag{9}$$

The flexural elastic modulus was obtained by the non-destructive impulse excitation method (Sonelastic, ATCP, ASTMC 747, Brazil) using bar-shaped samples.

3. Results and Discussion

The solid-state reaction that forms CA_6 is a double-diffusion mechanism, where Ca^{2+}, Al^{3+}, and O^{2-} ions are mutually exchanged between particles. Since the diffusion rates of Ca^{2+} in Al_2O_3 and Al^{3+} in CaO are significantly different, the overall reaction kinetics is slow, and several intermediate compounds may be formed and decomposed before reaching the equilibrium composition[1,6,17,19]. The density of the intermediate compounds (C_3A = 3.15 g.cm^{-3}, CA = 2.9 g.cm^{-3}, and $C_{12}A_7$ = 2.6 g.cm^{-3}) have lower values than the reactants (Al_2O_3 = 3.9 g.cm^{-3}, CaO = 3.5 g.cm^{-3} and CA_6 = 3.2 g.cm^{-3}) and the volumetric expansion resulting from its formation tends to separate the grains and make densification slower. Due to this aspect and to the large plate-like morphology of CA_6 crystals, such structures are intrinsically densification-resistant[16-19].

In the samples produced with α-Al_2O_3, dehydration of the CAC hydrates occurs first (up to 400 °C), causing initial shrinkage[14]. As the temperature increases to 1500 °C, there is gradual volume expansion, as the formation of the $CaAl_4O_7$ (CA_2) phase is completed. Eventually, some shrinkage occurs between 1500 and 1650 °C due to densification. This result suggests that all the samples were well crystallized, and their formation process was completed, as shown in Figure 1

The CA_6 samples produced in this work showed very similar real density values (~3.8 g.cm^3), as shown in Table 2

3.1. Uniaxial compression resistance and apparent porosity

The uniaxial compressive strength and apparent porosity results (Figure 2) show that the samples produced with ρ-Al_2O_3 presented higher apparent porosity, both for green

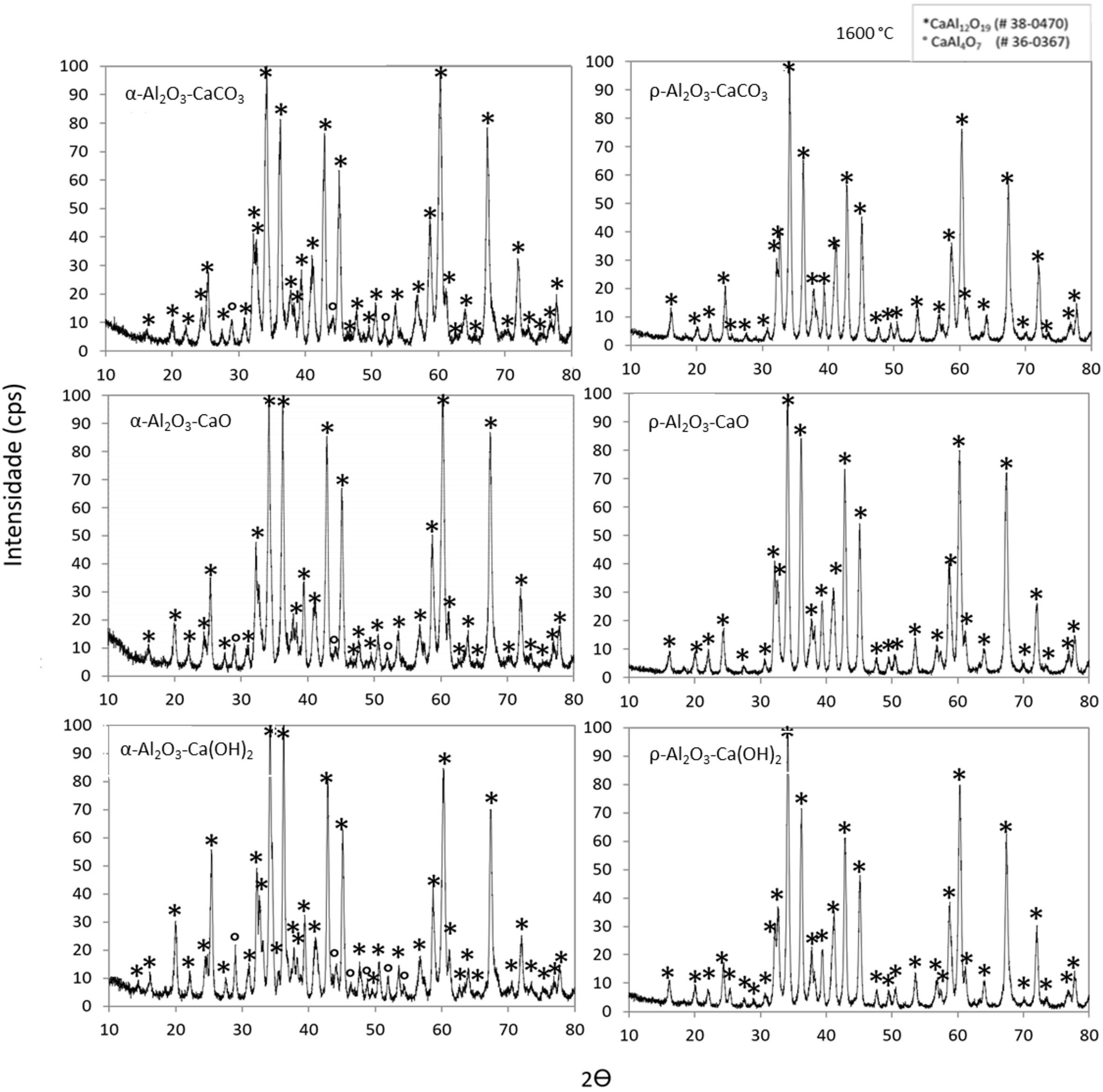

Figure 1. DRX pattern for samples CA_6 obtained by direct molding from compositions of α-Al_2O_3 and ρ-Al_2O_3 with different calcium sources sintered at 1600 °C. Identified phases $CaAl_{12}O_{19}$ (JCPDS 38-0470) and $CaAl_4O_7$ (JCPDS 36-0367).

Table 2. Real density of CA_6 samples obtained by direct molding from α-Al_2O_3 and ρ-Al_2O_3 compositions with different calcium sources sintered at 1550°C and 1600°C.

Al_2O_3 Precursors	CaO Precursors		$Ca(OH)_2$ ($g.cm^{-3}$)
	$CaCO_3$ ($g.cm^{-3}$)	CaO ($g.cm^{-3}$)	
α-Al_2O_3 (1550/1600)	3.79/3.79	3.80/3.80	3.78/3.79
ρ-Al_2O_3 (1550/1600)	3.78/3.79	3.78/3.79	3.78/3.78

or sintered samples and, consequently, a lower uniaxial compressive strength than those prepared with α-Al_2O_3.

Regarding the alumina source, all samples prepared with ρ-Al_2O_3 presented higher apparent porosity (approximately 65%) than those prepared with α-Al_2O_3 (approximately 25%, Figure 2). The ρ-Al_2O_3 composition has some peculiar characteristics that affect its density, such as a significantly lower packing efficiency than α-Al_2O_3, lower density, and the presence of 10-15 wt.% of chemically bound water, generating green bodies with higher porosity than those obtained with α-Al_2O_3. This behavior can be explained by the greater water consumption in the preparation of ρ-Al_2O_3 suspensions

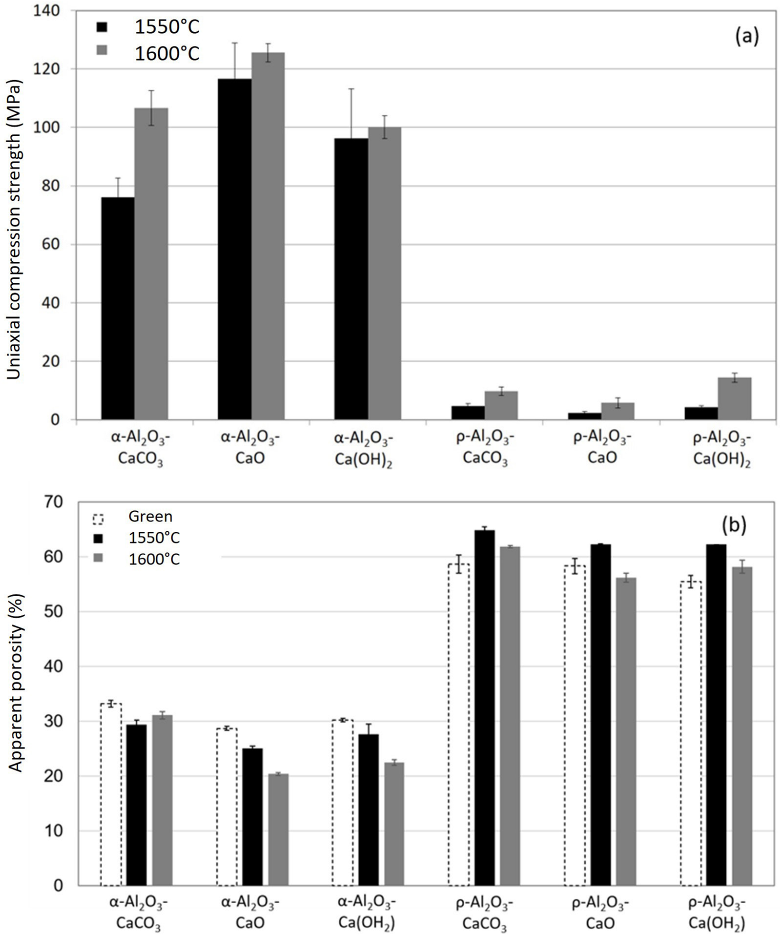

Figure 2. (a) Uniaxial compression strength and (b) apparent porosity of samples CA_6 obtained by direct molding from compositions of α-Al_2O_3 and ρ-Al_2O_3 with different calcium sources sintered at 1550 °C and 1600 °C.

(Table 1) as well as the dehydroxylation of the binder because pores formed spontaneously as the mixing water is vaporized and the hydrated phases decompose during calcination. It is worth mentioning that the transformation from ρ-Al_2O_3 to α-Al_2O_3 at higher temperatures involves the formation of other transition phases. For example, above 250 °C ρ-Al_2O_3 transforms firstly into boehmite and other metastable phases as temperature rises. Similar results were observed for other CaO-free ρ-Al_2O_3-bonded castable systems. During such phase transitions, the increase in density (from 3.2 $g.cm^{-3}$ to 3.8 $g.cm^{-3}$) behaves as a porogenic mechanism, whereas the decomposition of alumina hydrates creates an additional porosity in the matrix. It has been reported that the open porosity of CA_6 produced from ρ-Al_2O_3 compositions is approximately 60%[66,67]. Specifically, for the ρ-Al_2O_3-$CaCO_3$ composition sintered at 1600 °C, the open porosity reached 62.7%.

Some reactions occur in an α-Al_2O_3-$CaCO_3$ matrix with increasing temperature, leading to the formation of pores and intermediate phases, following a few steps. At room temperature (T = 25 °C), the suspension consists of the main matrix (α-Al_2O_3) and $CaCO_3$ aggregates that contain closed pores. In the temperature range of 500 - 900 °C, $CaCO_3$ decomposes, releasing carbon dioxide (CO_2), forming the first open pores[17,19]. Between 1100 and 1362 °C, the $C_{12}A_7$ and CA phases are formed, along with a small amount of liquid phase at the interface with the alumina matrix due to the melting of the $C_{12}A_7$ phase. As the temperature rises to 1400 °C, more alumina dissolves into the CA phase and the formation of the CA_2 phase begins. Between 1400 and 1500 °C, CA_2 reacts with the alumina excess, and the CA_6 phase is formed. At temperatures above 1500 °C, the CA_6 phase stabilizes in terms of microstructure and pore volume.

According to the literature, the total porosity (TP) of CA_6 produced by the α-Al_2O_3–$CaCO_3$ route was 50.5 ± 0.5%. For the samples sintered at 1600 °C produced in this work, the results of volumetric density (VD), and total porosity (TP) are presented in Table 3. The samples produced with α-Al_2O_3 presented porosity of around 40%, while the samples produced with α-bond reached around 67% of porosity, except for the sample produced with CaO, which displayed 62% porosity.

3.2. Pore size distribution

Figure 3 shows the pore size distribution of samples produced with the compositions containing α-Al_2O_3 and ρ-Al_2O_3.

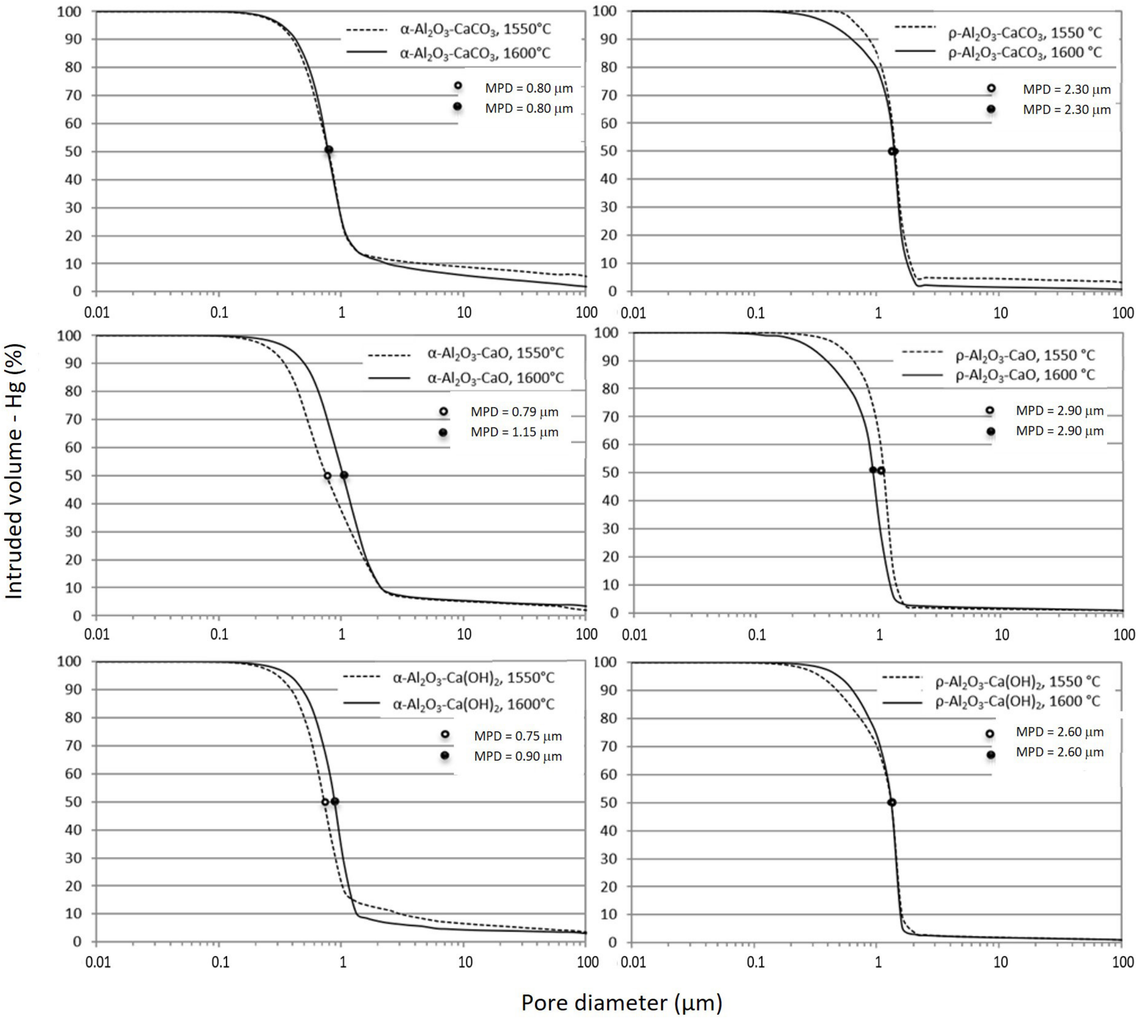

Figure 3. Pore size distribution of CA_6 samples obtained by direct molding from α-Al_2O_3 and ρ-Al_2O_3 compositions with different calcium sources after sintering at 1550°C and 1600°C.

Table 3. Volumetric density (VD), and total porosity (TP) of the CA_6 samples sintered at 1600 °C.

Compositions	VD (g.cm^{-3})	TP (%)
α-Al_2O_3-$CaCO_3$	2.285	41.2
α-Al_2O_3-CaO	2.367	39.1
α-Al_2O_3-$Ca(OH)_2$	2.382	38.8
ρ-Al_2O_3-$CaCO_3$	1.295	66.7
ρ-Al_2O_3-CaO	1.462	62.4
ρ-Al_2O_3-$Ca(OH)_2$	1.261	67.6

CA_6, when produced with compositions α-Al_2O_3, presented a smaller average pore diameter (APD), in the range of 0.75 and 1.15 μm, when compared to ρ-Al_2O_3, in the range of 2-3 μm. This occurs due to the packing of the particles, which is facilitated by the size of the grains and the intertwining between them in the crystalline structure, resulting in a smaller percentage of pore volume compared to ρ-Al_2O_3. This can be explained by the greater difference in particle size between ρ-Al_2O_3 and CaO when compared to the significantly smaller particle size difference between α-Al_2O_3 and CaO. Because hydratable alumina presents a larger average particle size compared to the CaO, its packing

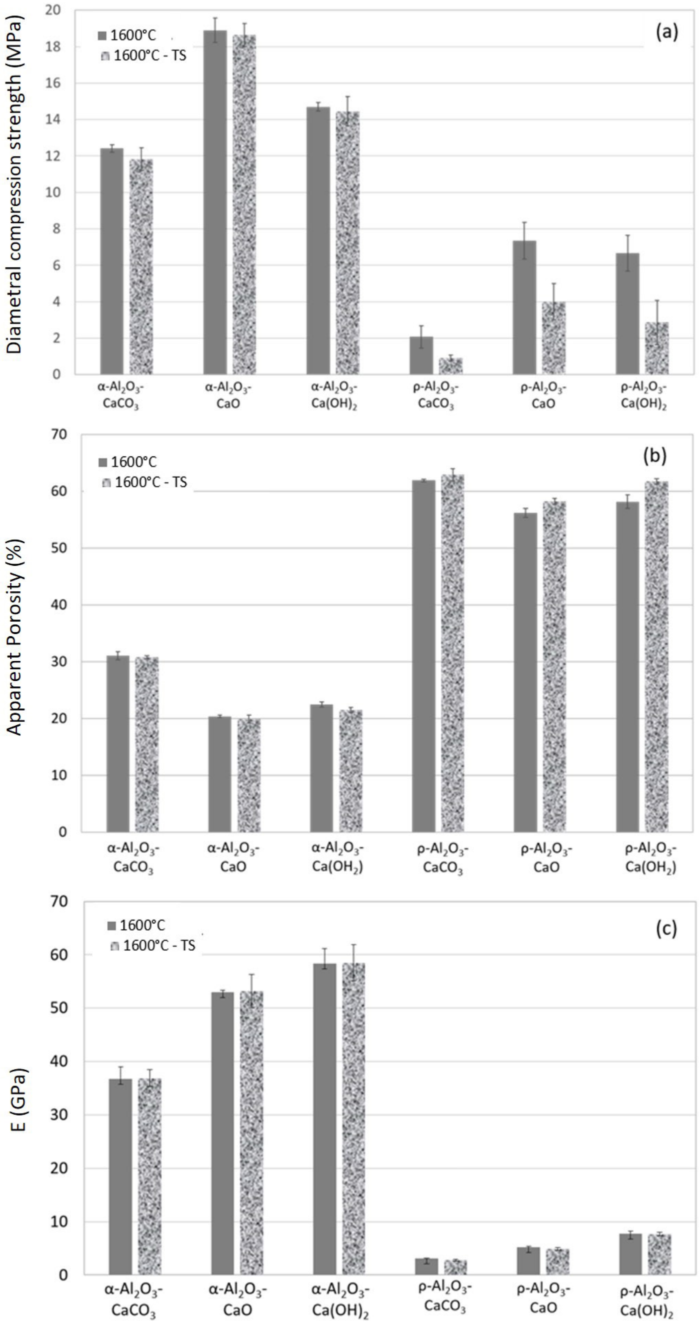

Figure 4. (a) Diametral compression strength, (b) apparent porosity, and (c) elastic modulus of samples CA$_6$ obtained by direct molding from compositions of α-Al$_2$O$_3$ and ρ-Al$_2$O$_3$ with different calcium sources, sintered at 1600 °C before and after thermal shock procedure.

efficiency is significantly lower which generates higher pore size in the samples. Another factor that contributes to the quantity and size of pores is the percentage of water in the composition during sample preparation, which is released as vapor during the sintering process leaving voids and small pores. Samples α-Al$_2$O$_3$-CaCO$_3$ presented a platelet structure, whereas for the ρ-Al$_2$O$_3$-CaCO$_3$ ones, a more equiaxial morphology in grains with curved boundaries and higher porosity and consequently lower mechanical properties.

3.3. Diametral compression strength, apparent porosity, and elastic modulus after thermal shock

Samples' diametric compression strength, apparent porosity, average pore size, and elastic modulus measured before and after 10 cycles of heating and cooling are presented in Figures 4 and 5. Samples showed very similar levels of total porosity, apparent density, and average pore diameters before

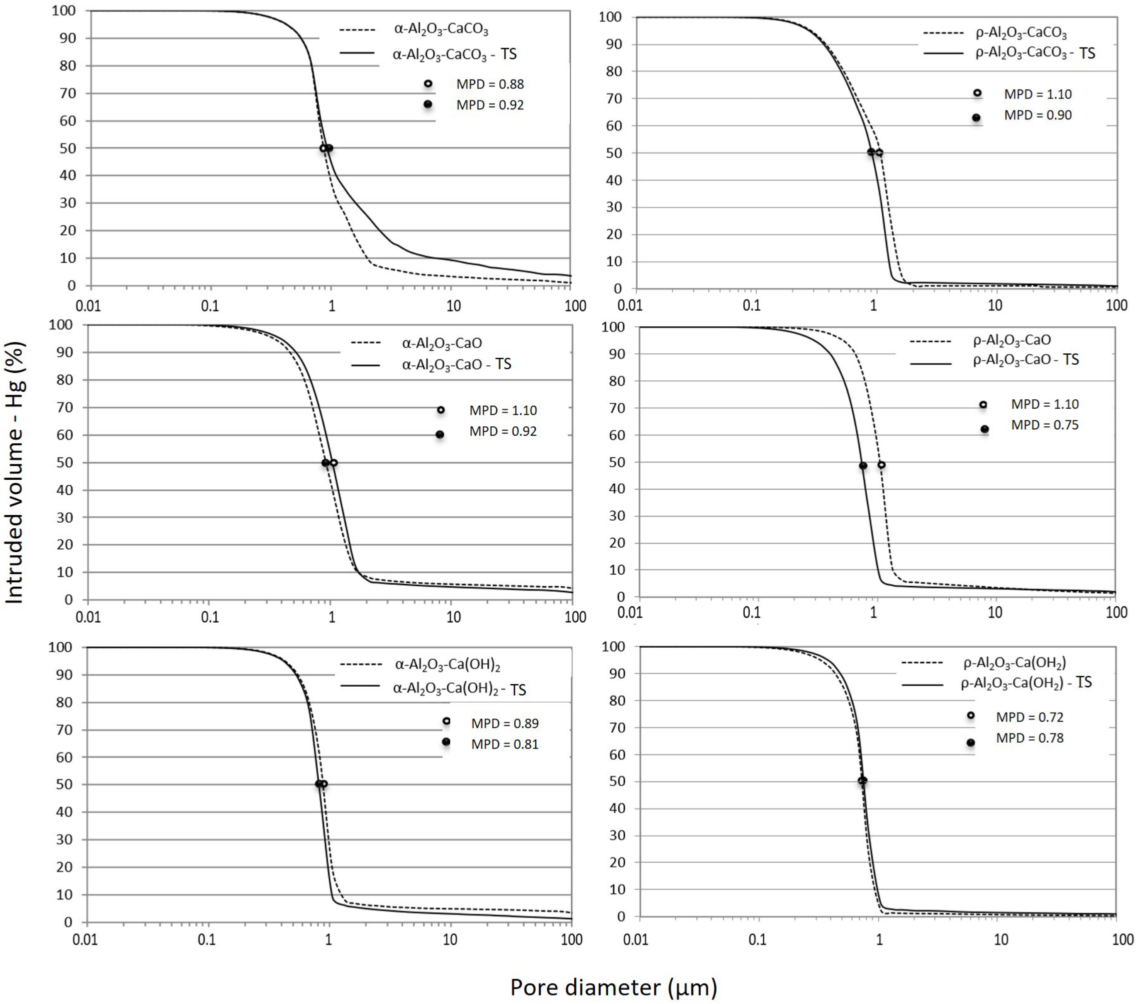

Figure 5. Pore size distribution of samples CA_6 obtained by direct molding from α-Al_2O_3 and ρ-Al_2O_3 compositions with different calcium sources, sintered at 1600 °C before and after thermal shock procedure.

and after the procedure. The porous structure of the material proved to be very stable and was not significantly affected by thermal shock. The small diameter pores contributed to the material's low thermal conductivity and its resistance to thermal shock[10,12,13,53,63].

The lamellar shape of crystals CA_6 can behave as a toughening mechanism, promoting crack deflection and grain interlocking to reduce damage by thermal shock[2,3,9,21,22]. The results attained for α-Al_2O_3-containing compositions corroborate this information, as there was no significant strength variation before and after the thermal shock cycles. On the other hand, samples produced with ρ-Al_2O_3 had significant thermal shock damage, which is characterized as a strength reduction after thermal cycling. This behavior may be associated with the arrangement of the crystals in a house of cards, a structure that is not favorable to heat transport by radiation and results in low thermal conductivity at high temperatures (> 1000 °C), and the higher porosity and the reduced pore dimensions, as verified through Hg porosimetry tests. Scanning electron microscopy for samples sintered at 1600 °C is shown in Figure 6.

Assessment of the elastic modulus of ceramics using non-destructive tests is useful in determining its structural integrity[52,53]. This property is significantly affected by the presence of cracks or laminations and by the degree of connection between them. The employed technique involves the determination of resonance frequencies of harmonic waves induced in a bar employing a quick mechanical excitation. According to the literature, the reduction in elastic modulus after a thermal shock cycle is associated with the spontaneous formation of microscopic cracks in ceramic samples. However, when the pores are randomly distributed, the effects of porosity interfere as little as possible with elastic modulus, which explains why the samples did not show changes in modulus after thermal shock[65,66,68,69].

Thermal shock damage, when not catastrophic, is more intense at the surface of the material. This explains the reduction of mechanical strength after the thermal shock cycles since surface cracks control this property. On the other hand, porosity and elastic modulus are associated with the bulk sample, in which microstructure remained practically unchanged after thermal shock cycles.

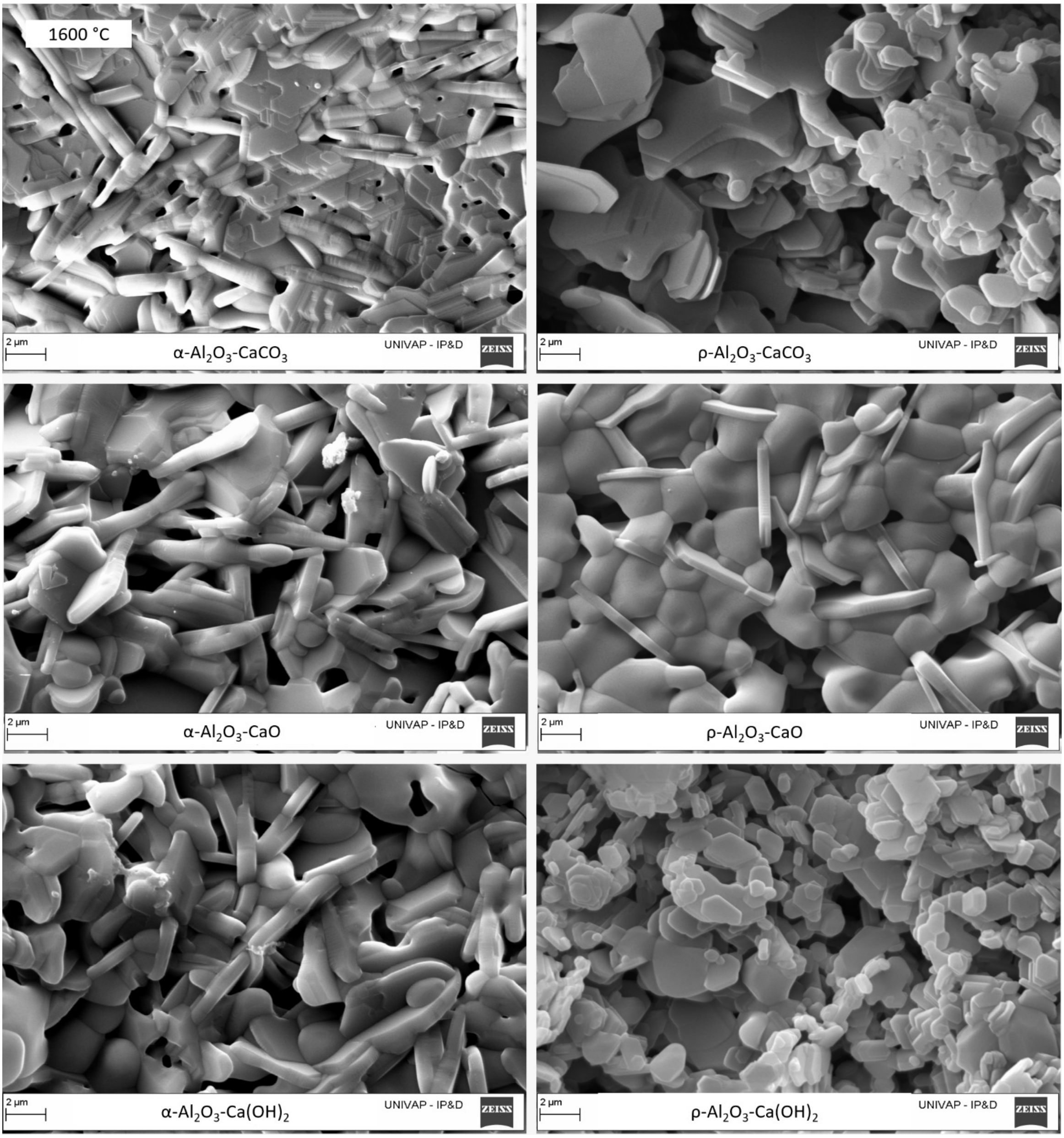

Figure 6. Scanning electron microscopy of samples CA_6 obtained by direct molding from α-Al_2O_3 and ρ-Al_2O_3 compositions with different calcium sources, sintered at 1600 °C before thermal shock procedure.

4. Conclusions

Calcium hexaluminate (CA_6) samples prepared with ρ-Al_2O_3 present much lower uniaxial and diametral compression strength and elastic modulus when compared to those prepared with α-Al_2O_3, regardless of the calcium source, which is by the higher apparent porosity (approximately 65%) verified for these samples when comparing the α-Al_2O_3 compositions (approximately 25%), which can be correlated to the higher water consumption in the preparation of ρ-Al_2O_3 suspensions. Such samples CA_6 also have larger pores (in the range of 2 to 3 μm) when compared to α-Al_2O_3 compositions (in the range of 0.8 to 1.2 μm). The same behavior about the raw materials used was verified after the thermal shock procedure and it was verified that the samples produced were resistant to the procedure. The lamellar shape of particles CA_6 (mainly in α-Al_2O_3) favors anchoring, improving mechanical performance, with the route with CaO being the one with the highest values, showing that it is possible to synthesize CA_6 using a more environmentally friendly system.

5. Acknowledgments

The authors would like to acknowledge the Brazilian Research Foundations: FAPESP #2015/01541-0 and

#2010/19274-5, CNPq and Finep for supporting this research and Multi-User Analytical Center of Univap.

6. References

1. Gentile AL, Foster WR. Calcium hexaluminate and its stability relations in the system CaO–Al2O3–SiO2. J Am Ceram Soc. 1963;46(2):74-6.
2. Nagaoka T, Kanzaki S, Yamaoka Y. Mechanical properties of hot-pressed calcium hexaluminate ceramics. J Mater Sci Lett. 1990;9(2):219-21.
3. An L, Chan HM, Soni KK. Control of calcium hexaluminate grain morphology in in-situ toughened ceramic composites. J Mater Sci. 1996;31(12):3223-9.
4. Asmi D, Low IM. Physical and mechanical characteristics of in-situ alumina/calcium hexaluminate composites. J Mater Sci Lett. 1998;17(20):1735-8.
5. Sánchez-Herencia AJ, Moreno R, Baudín C. Fracture behavior of alumina-calcium hexaluminate composites obtained by colloidal processing. J Eur Ceram Soc. 2000;20(14-15):2575-83.
6. Domínguez C, Chevalier J, Torrecillas R, Fantozzi G. Microstructure development in calcium hexaluminate. J Eur Ceram Soc. 2001;21(3):381-7.
7. Vázquez BA, Pena P, Aza AH, Sainz MA, Caballero A. Corrosion mechanism of polycrystalline corundum and calcium hexaluminate by calcium silicate slags. J Eur Ceram Soc. 2009;29(8):1347-60.
8. Zacherl D, Kockegey-Lorenz R, Buhr A. Industrial application experiences with microporous calcium hexaluminate insulating material SLA-92. In: TMS Annual Meeting; 2010; Seattle, WA. Proceedings. Warrendale, PA: TMS; 2010. pp. 99-109.
9. Zacherl D, Schnabel M, Buhr A, Büchel G, Kockegey-Lorenz R, Dutton J. Advantages of calcium hexaluminate in a corrosive environment. In: Materials Science and Technology Conference and Exhibition; 2011; Columbus, Ohio, USA. Proceedings. New York: Curran Associates, Inc.; 2011. pp. 76-86.
10. Costa LMM, Sakihama J, Salomão R. Characterization of porous calcium hexaluminate ceramics produced from calcined alumina and microspheres of Vaterite (μ-CaCO3). J Eur Ceram Soc. 2018;38(15):5208-18.
11. Sakihama J, Salomão R. Microstructure development in porous calcium hexaluminate and application as a high-temperature thermal insulator: a critical review. Interceram. 2019;68:58-65.
12. Salomão R, Oliveira K, Fernandes L, Tiba P, Prado U. Porous refractory ceramics for high-temperature thermal insulation - part 2: the technology behind energy saving. Interceram. 2022;71(1):38-50.
13. Salomão R, Fernandes L, Prado US, Tiba P. Porous refractory ceramics for high-temperature thermal insulation - part 3: innovation in energy saving. Interceram. 2022;71(3):30-7.
14. Salomão R, Kawamura MA, Emilio ABV, Sakihama J, Segadães AM. Calcium aluminate cement in castable alumina: from hydrate bonding to the in-situ formation of calcium hexaluminate. Ceram Int. 2021;47(11):15082-93.
15. MacKenzie KJD, Schmücker M, Smith ME, Poplett IJF, Kemmitt T. Evolution of crystalline aluminates from hybrid gel-derived precursors studied by XRD and multinuclear solid state MAS NMR IV: Calcium dialuminate, CaAl$_4$O$_7$ and calcium hexaluminate, CaAl12O19. Thermochim Acta. 2000;363(1-2):181-8.
16. Tulliani JM, Pagès G, Fantozzi G, Montanaro L. Dilatometry as a tool to study a new synthesis for calcium hexaluminate. J Therm Anal Calorim. 2003;72(3):1135-40.
17. Salomão R, Ferreira VL, de Oliveira IR, Souza ADV, Correr WR. Mechanism of pore generation in calcium hexaluminate (CA6) ceramics formed in situ from calcined alumina and calcium carbonate aggregates. J Eur Ceram Soc. 2016;36(16):4225-35.
18. Khajornboon J, Ota K, Washijima K, Shiono T. Control of hexagonal plate-like microstructure of in-situ calcium hexaluminate in monolithic refractories. J Asian Ceram Soc. 2018;6(3):196-204.
19. Salomão R, Ferreira VL, Costa LMM, de Oliveira IR. Effects of the initial CaO-Al2O3 ratio on the microstructure development and mechanical properties of porous calcium hexaluminate. Ceram Int. 2018;44(2):2626-31.
20. An L, Ha HC, Chan HM. High-strength alumina/alumina: calcium-hexaluminate layer composites. J Am Ceram Soc. 1998;81(12):3321-4.
21. Domínguez C, Chevalier J, Torrecillas R, Gremillard L, Fantozzi G. Thermomechanical properties and fracture mechanisms of calcium hexaluminate. J Eur Ceram Soc. 2001;21(7):907-17.
22. Khajornboon J, Washijima K, Shiono T. Fracture energy and fracture toughness of in situ calcium hexaluminate (CA6)-Alumina monolithic refractory. Key Eng Mater. 2018;766:77-82.
23. Dong B, Wang F, Yu J, Abadikhah H, Khan SA, Yang M, et al. Production of calcium hexaluminate porous planar membranes with high morphological stability and low thermal conductivity. J Eur Ceram Soc. 2019;39(14):4202-7.
24. Yuan L, Yao X, Yan Z, Jin E, Li C, Liu Z, et al. Preparation and characterization of calcium hexaaluminate (CA6) porous ceramic for application in high-temperature flue gas filtration. Journal of the Australian Ceramic Society. 2022;58(5):1701-8.
25. Li S, Chen D, Fu L, Zou Y, Huang A, Gu H. Gas corrosion behavior of calcium hexaluminate materials for hydrogen metallurgy. Ceram Int. 2023;49(10):15787-92.
26. Asmi D, Low IM. Processing of an in-situ Layered and Graded Alumina/Calcium-Hexaluminate composite: physical Characteristics. J Eur Ceram Soc. 1998;18(14):2019-24.
27. Asmi D, Low IM, Kennedy S, Day RA. Characteristics of a layered and graded alumina/calcium-hexaluminate composite. Mater Lett. 1999;40(2):96-102.
28. Asmi D, Low IM, O'Connor BH, Buckley C. Phase compositions and depth-profiling of calcium aluminates in a functionally graded alumina/calcium-hexaluminate composite. J Mater Process Technol. 2001;118(1-3):219-24.
29. Singh M, Low IM, Asmi D. Depth profiling of a functionally graded alumina/calcium-hexaluminate composite using grazing incidence synchrotron-radiation diffraction. J Eur Ceram Soc. 2002;22(16):2877-82.
30. Yi S, Liu YG, Fang MH, Li WJ, Huang ZH. Effect of sintering temperature on phase composition, microstructure and properties of calcium hexaluminate refractory. Interceram, 2010;59(3-4):56-58, .
31. De La Iglesia PG, García-Moreno O, Torrecillas R, Menéndez JL. Influence of different parameters on calcium hexaluminate reaction sintering by Spark Plasma. Ceram Int. 2012;38(7):5325-32.
32. Kawaguchi K, Suzuki Y, Goto T, Cho SH, Sekino T. Homogeneously bulk porous calcium hexaaluminate (CaAl$_{12}$O$_{19}$): reactive sintering and microstructure development. Ceram Int. 2018;44(4):4462-6.
33. Nagaoka T, Tsugoshi T, Hotta Y, Yasuoka M, Watari K. Forming and sintering of porous calcium-hexaaluminate ceramics with hydraulic alumina. J Mater Sci. 2006;41(22):7401-5.
34. Oliveira IR, Leite VMC, Lima MPVP, Salomão R. Production of porous ceramic material using different sources of alumina and calcia. Revista Materia. 2015;20(3):739-46.
35. Salomão R, Poiani AJB, Costa LMM. Porous beads of in-situ calcium hexaluminate prepared by extrusion-dripping. Interceram. 2019;68(3):40-9.
36. Yi S, Huang Z, Huang J, Fang M, Liu Y, Zhang S. Novel calcium hexaluminate/spinel-alumina composites with graded microstructures and mechanical properties. Sci Rep. 2014;4:4333.
37. Tomba Martinez AG, Luz AP, Braulio MAL, Sako EY, Pandolfelli VC. Revisiting CA$_6$ formation in cement-bonded alumina-spinel refractory castables. J Eur Ceram Soc. 2017;37(15):5023-34.
38. Feng X, Li W, Guo H, Cao J, Liu B, Hou Y, et al. Low-temperature fabrication and properties of porous calcium hexaluminate

(CA6) ceramics with low thermal conductivity by one-step method. Ceram Int. 2023;49(6):9789-98.

39. Pan L, Li Y, Tan F, Wang Q, Chen Y, Wang Q, et al. Influence of calcium hexaluminate gradation on interfacial microstructure and fracture behavior of cement-bonded alumina castables. Ceram Int. 2023;49(10):16137-48.
40. Yuan L, Jin E, Li C, Liu Z, Tian C, Ma B, et al. Preparation of calcium hexaluminate porous ceramics by novel pectin based gelcasting freeze-drying method. Ceram Int. 2021;47(7):9017-23.
41. Wang S, Yang Z, Luo X, Qi X, Zhang L, You J. Preparation of calcium hexaluminate porous ceramics by gel-casting method with polymethyl methacrylate as pore-forming agent. Ceram Int. 2022;48(20):30356-66.
42. Li L, Yan Y, Fan X, Hu Z, Zhao C. Low-temperature synthesis of calcium-hexaluminate/magnesium-aluminum spinel composite ceramics. J Eur Ceram Soc. 2015;35(10):2923-31.
43. Zhao Y, Shi G, Miao J, Liu R, Sang X. Preparation of hierarchically porous calcium hexaaluminate ceramics through in-situ gelation-assisted direct ink writing. Ceram Int. 2024;50(8):13634-43.
44. Liu J, Gu H, Zhang M, Huang A, Li H. Improvement in fatigue resistance performance of corundum castables with addition of different size calcium hexaluminate particles. Ceram Int. 2019;45(1):225-32.
45. Zhao F, Ge T, Zhang L, Xu E, Gao J, Liu X. A novel method for the fabrication of porous calcium hexaluminate (CA6) ceramics using pre-fired CaO/Al$_2$O$_3$ pellets as calcia source. Ceram Int. 2020;46(4):4762-70.
46. Chen A, Li L, Ren W, Wang C, Wang Q. Influence of MgO-Al$_2$O$_3$ hollow sphere content on the microstructure and mechanical properties of calcium hexaluminate porous ceramics. J Asian Ceramic Soc. 2024;12(1):59-70.
47. Salvini VR, Luz AP, Pandolfelli VC. High temperature Al$_2$O$_3$-CA$_6$ insulating foamed ceramics: processing and properties. Interceram. 2012;61(6):335-9.
48. Wu M, Li Y, Li S, Li Y, Sang S. Preparation and properties of high-purity porous calcium hexaluminate material. Key Eng Mater. 2016;697:547-50.
49. Finhana IC, Machado VVS, Santos T Jr, Borges OH, Salvini VR, Pandolfelli VC. Direct foaming of macroporous ceramics containing colloidal alumina. Ceram Int. 2021;47(11):15237-44.
50. Sarpoolaky H, Ahari KG, Lee WE. Influence on in situ phase formation on microstructural evolution and properties of castable refractories. Ceram Int. 2002;28(5):487-93.
51. Overhoff AB, Grass J, Wuthnow HM. New microporous materials. Ceram Forum Int. 2005;82(8):1-5.
52. Alex J, Vandeperre L, Lee WE, Touzo B, Parr C. Effect of sodium on microstructures and thermoelastic properties of calcium aluminate cement-bonded refractories. J Am Ceram Soc. 2016;99(3):1079-85.
53. Luz AP, Salomão R, Bitencourt CS, Renda CG, Lucas AA, Aneziris CG, et al. Thermosetting resins for carbon-containing refractories: theoretical basis and novel insights. Open Ceram. 2020;3:100025.
54. Cinibulk MK. Effect of precursors and dopants on the synthesis and grain growth of calcium hexaluminate. J Am Ceram Soc. 1998;81(12):3157-68.
55. Sako EY, Braulio MAL, Milanez DH, Brant PO, Pandolfelli VC. Microsilica role in the CA$_6$ formation in cement-bonded spinel refractory castables. J Mater Process Technol. 2009;209(15-16):5552-7.
56. Hu M, Fang M, Cheng S, Yang T, Huang Z, Liu Y. Effects of calcium hexaluminate addition on the mechanical properties of zirconia-toughened-alumina. Key Eng Mater. 2012;544:286-90.
57. Dong B, Yuan B, Wang G, Chen K, Han J, Li H. Fabrication of porous SiC/calcium hexaluminate composites. J Eur Ceram Soc. 2016;36(16):3889-93.
58. Qiong L, Huazhi G, Yalan Y, Ao H, Meijie Z, Zhian L. Effect of SiO$_2$ micropowder on properties of calcium hexaluminate castables for coal catalytic gasifiers. Interceram. 2018;67(1):32-7.
59. Li Y, Xiang R, Xu N, Wang Q, Li S, Wu M, et al. Fabrication of calcium hexaluminate-based porous ceramic with microsilica addition. Int J Appl Ceram Technol. 2018;15(4):1054-9.
60. Wu J, Zhang C, Xu X, Liu X, Zhou S. Preparation and characterization of alumina/calcium-hexaluminate ceramic composites from ferrotitanium slag. J Eur Ceram Soc. 2020;40(12):4265-75.
61. Salomão R, Arruda, CC, Pandolfelli VC, Fernandes L. Designing high-temperature thermal insulators based on densification-resistant in situ porous spinel. J Eur Ceram Soc. 2021;41(4):2923-37.
62. Li B, Li G, Chen H, Chen J, Hou X, Li Y. Physical and mechanical properties of hot-press sintering ternary CM$_2$A$_8$ (CaMg$_2$Al$_{16}$O$_{27}$) and C$_2$M$_2$A$_{14}$ (Ca$_2$Mg$_2$A$_{128}$O$_{46}$) ceramics. Journal of Advanced Ceramics. 2018;7(3):229-36.
63. Hammel EC, Ighodaro OL, Okoli OI. Processing and properties of advanced porous ceramics: an application-based review. Ceram Int. 2014;40(10):15351-70.
64. Salomão R, Pandolfelli VC. Polypropylene fibers and their effect on processing refractory castables. Int J Appl Ceram Technol. 2007;4(6):496-502.
65. ASTM: American Society for Testing and Materials. ASTM C1525 03: standard test method for determination of thermal shock resistance for advanced ceramics by water quenching. West Conshohocken: ASTM; 2003.
66. Souza ADVD, Sousa LLD, Fernandes L, Cardoso PHL, Salomão R. Al$_2$O$_3$–Al (OH) 3-based castable porous structures. J Eur Ceram Soc. 2015;35(6):1943-54.
67. Salomão R, Kawamura MA, Souza ADVD, Sakihama J. Hydratable alumina-bonded suspensions: evolution of microstructure and physical properties during first heating. Interceram. 2017;66:28-37.
68. Li Y, Li X, Zhu B, Chen P. The relationship between the pore size distribution and the thermo-mechanical properties of high alumina refractory castables. Int J Mater Res. 2016;107:263-8.
69. Tallon C, Chuanuwatanakul C, Dunstain DE, Franks GV, Mechanical strength, and damage tolerance of highly porous alumina ceramics produced from sintered particle stabilized foams. Ceram Int. 2016;42:8478-87.